Program Digest, 2019 IEEE International Ultrasonics Symposium (IUS)
Glasgow, Scotland, October 6-9, 2019

Vector Flow Velocity Estimation from Beamsummed Data Using Deep Neural Networks

You Leo Li, Dongwoon Hyun, Jeremy J. Dahl
Department of Radiology
School of Medicine, Stanford University
Palo Alto, California, USA
Email: leo.you.li@stanford.edu

***Abstract*—Vector flow imaging (VFI) is a novel velocity measurement technique that provides flow velocity information in both azimuth and axial dimensions. Compared to conventional color Doppler imaging, VFI provides velocity estimation that is independent of flow directions. Previous VFI techniques utilize either multiple transmit or receive beams or angles, or speckle tracking. This creates a trade-off between computational intensity and estimate quality or equipment cost. In this work, we present a vector flow velocity estimation technique based on deep neural networks using only beamsummed radio-frequency (RF) data. The deep neural network extracts features from the RF data, and performs flow velocity estimation on the features, and maps the estimates back to the spatial domain. The structure and training of the neural network model is presented. The performance of the technique is demonstrated and evaluated using simulations and flow phantom experiments.**

***Index Terms*—Ultrasonic imaging, Doppler, Neural networks**

I. Introduction

Vector flow imaging (VFI) provides estimation of blood flow velocities in both azimuth and axial dimensions. Compared to conventional color Doppler imaging that only estimates flow velocities along ultrasound beam directions, VFI is able to provide two-dimensional (2D) velocity estimation that is independent of flow directions. It has promising applications in the measurement of complex flow patterns, including cardiac flow [1]. Conventional VFI can be achieved using multiple angles in either transmit or receive [2]–[4], or through specking tracking [5]. Despite their success, they are computationally intensive and efforts to improve computational efficiency may sacrifice estimate quality or equipment cost.

In this work, we propose and demonstrate a vector flow estimation technique based on a deep neural network using only beamsummed RF data. After clutter filtering, the beamsummed RF image frames of two consecutive Doppler acquisitions are used for each estimation. The network extracts feature from the RF signals, performs estimation of flow in the feature space, and maps the estimate back to the spatial domain. The estimated results can be further processed. The network was trained using a multi-stage method with simulated flow data.

The performance of the method is demonstrated using Field II simulation studies [6], [7] with a parabolic velocity profile and various peak flow velocities and angles and a flow phantom experiment using a Verasonics Vantage 256 scanner and a C5-2v transducer.

Research reported in this publication was funded through the Human Placenta Project, an initiative supported by the Eunice Kennedy Shriver National Institute Of Child Health and Human Development of the National Institutes of Health under award number R01-HD086252.

II. Methods

A. Neural Network Structure and Pre-training Methods

The neural network utilized for the work is the PWC-Net that has five major components: feature pyramid, warping layer, cost volume layer, optical flow estimator, and context layer [8]. Detailed descriptions of the components can be found in Sun et al. [8] and is summarized below.

The inputs to the neural network are two frames of beamsummed radio-frequency (RF) data acquired using two consecutive Doppler packets. Each frame has azimuth and axial dimensions. The feature pyramid, which is a 6-level convolutional neural network, extracts features from two input frames. A cost volume layer computes the matching cost between the features extracted from the two frames. The matching cost and the features are then used as inputs to a optical flow estimation layer to produce a coarse estimation of flow. The flow and the features are used in a warping layer, which performs bilinear interpolation of the features extracted from the second frame using the coarsely estimated flow information. The process is repeated once, so that a fine estimation of flow can be produced. Post-processing of the estimated flow is conducted by the context network, which is a 7-layer feed-forward dilated convolutional network that exploits contextual information and refines details.

The the neural network was first pre-trained by Sun et al. [9] with a multi-stage process on large-scale open datasets, including FlyingChairs [10], FlyingThings3D [10], KITTI [11], and MPI Sintel [12]. The details of the pre-training methods and performance evaluation on open datasets are presented in Sun et al. [9]. The pre-training using the large-scale data sets is critical to the performance of the network.

B. Fine-tuning Methods and Simulation Study Methods

The pre-trained network was fine-tuned with simulated ultrasonic Doppler data to improve its performance in flow estimation.

The ultrasonic Doppler flow data were simulated using Field II [6], [7] simulation tool with similar methods as reported previously [13], [14]. A total of 90 different imaging cases were generated with randomly determined blood vessel diameters, vessel angles, and peak velocity magnitudes. In each simulation case, an 8 MHz, 0.2 mm pitch, 128 element linear transducer was used for transmit and receive, and a longitudinal cross-sectional view at the center cross-section of the vessel was used as the field-of-view (FOV). The vessels were embedded in homogeneous scatterers at a 3 cm depth. The diameters of the vessels were randomly generated using a uniform distribution between 1 and 3 mm. The angles of the vessels to the transducer axis were uniformly distributed between 0 and 360 degree. To simulate blood, scatterers within the vessel were given a scattering amplitude 60 dB lower than the surrounding tissue scatterers. Blood flow was simulated with the scatterers moving inside the simulated vessels with parabolic velocity profiles to represent fully developed laminar flow. The peak velocities at the center of the vessels are uniformly distributed between 0 and 50 mm/s along the vessel axis. The scatterer density for both the blood and the surrounding tissue was 20 scatterers per resolution voxel.

A plane wave synthetic transmit focusing (PWT) sequence [15] imaging sequences was utilized in the simulations. The pulse sequence uses 3-cycle pulses for transmit. For each Doppler packet, the PWT sequences fires 5 transmit plane waves with an angular spacing of 5 degrees, covering a $\pm 10°$ range. The plane wave firing frequency is 5 kHz, corresponding to a Doppler pulse repetition frequency of 1 kHz [16]. The received radio-frequency (RF) channel data acquired from different transmits were first sampled at 40 MHz and dynamically focused on receive. The focused channel data were then added coherently in the receive channel dimension and transmit angle dimension to produce beamsummed RF data. An ensemble length of 10 was obtained for each simulation case. Thermal noise was simulated by adding white Gaussian noise at levels of -20 to 20 dB relative to the blood signal (i.e. -80 to -40 dB relative to the stationary tissue signal). A 2-tap projection-initialized Butterworth filter [17], [18] with a cutoff frequency of 5 Hz was used to remove stationary clutter. The projection-initialization of the filter removes the components of the output signal in the transient subspace and improves the performance of the filters when only a small ensemble length is used [17]. For the simulation without tissue motion, the Butterworth filter with projection initialization is effective in removing stationary clutter.

The filtered beamsummed RF data were used for training, validation, and testing. As for the split of data, simulated data from 81 of the 90 cases were used for training. Validation set and testing set were comprised of data from 9 simulated cases each. After the fine-tuning, velocity estimation was performed on the test set, and the results were evaluated.

C. Flow Phantom Experiments

The performance of the neural network estimation were evaluated in flow phantom experiments. In the experiments, the flow was generated and controlled with an IDEX ISM596D flow pump (Oakharbor, WA 98277, USA) through an ATS flow phantom (Model 527, Bridgeport, CT, USA). The vessel in the flow phantom has a 2-mm-diameter and is at $18°$ relative to the phantom surface. The fluid utilized in the phantom was based on ATS Model 707 Doppler Test Fluid (Bridgeport, CT, USA) with 3% corn starch to simulate blood scattering. The volumetric velocity of the flow was directly controlled by the flow pump, and a range of $5 - 90\ mm^3/s$ was used in the experiments. The true volumetric flow velocity is measured using a timer and a balance.

The experiments were conducted with a Verasonics Vantage 256 research ultrasound scanner (Verasonics Inc., Redmond, WA, USA) and a C-2v curvilinear transducer. The imaging sequence utilized 5 diverging wave transmission waves at different steering angles [19]. The transmit phase delay is linear with respect to the transmit element number, covering a transmit angle range of $-15°$ to $15°$ with respect to transducer axis. For the Doppler acquisition, a Doppler pulse repetition frequency (PRF) of 1000 Hz was used to acquire Doppler data with an ensemble length of 512. Delay-compensated beamsummed RF data were acquired on the flow phantom, and filtered using a SVD-based spatiotemporal filter to remove stationary clutter [20]. The filtered beamsummed data was used as inputs to neural network velocity estimator to produce vector flow estimations. The estimation time is 0.11s for a pair of frames with 1024x128 spatial samples.

III. Results

A. Simulation Results

Fig. 1 shows an example of vector flow estimation using the neural network model on one simulation case that was not used in the training or validation. Fig. 1(a) shows the image of the entire field-of-view (FOV). The color of the vessel shows the magnitude of the velocity. The lengths of the blue arrows also shows the magnitude of the velocity, and the angles of the blue arrows show the direction of flow. Clear boundaries of the vessel and smooth flow velocity profile can be observed, except for near the two ends of the vessel, where the scatterers flow in and out of the FOV. Fig. 1(b) shows the velocity profiles at the axial cross-section at 3 mm in azimuthal dimension. The estimated azimuthal and axial flow velocities are shown in blue and red solid lines, respectively, and the ground truths are shown in dashed lines. The estimated velocities captures the parabolic velocity profile across the vessel.

Fig. 2 shows the estimated peak velocities with various simulated peak velocities. The results were obtained from the 9 simulated test cases. Each blue circle indicates the estimation on one test set simulation. The x-axis oindicates the true peak velocity for the simulation, and y-axis indicates the estimated peak velocity. The red dashed line shows where these two are equal.

B. Flow Phantom Experiments Results

Fig. 3 shows the velocity estimation from one experimental acquisition on the flow phantom. Fig. 3(a) shows the vector flow estimation image. Clear boundary between the vessel and the stationary phantom is visible in the image, and smooth

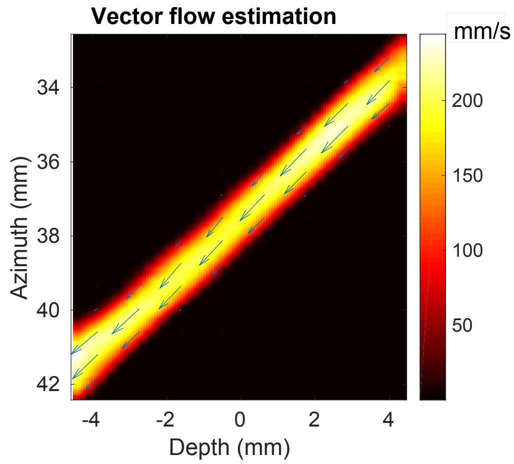

(a) Vector flow estimation results using one Field II simulation case in the test set. The estimated peak velocity is 211 mm/s, and the true velocity is 192 mm/s. The estimated flow angle is $-135.6°$ and the flow angle is $-137.5°$.

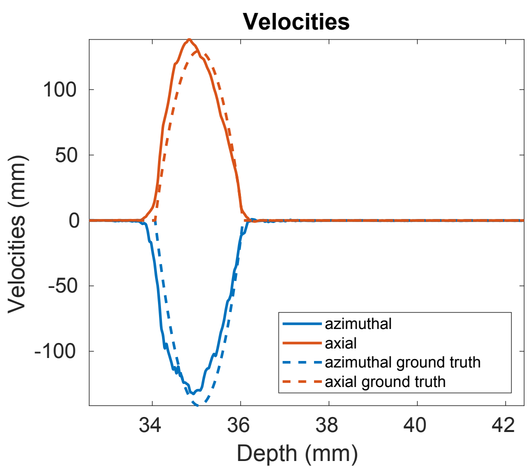

(b) Azimuth and axial velocities at the axial cross-section at 3 mm in the azimuth dimension, indicated with the white dashed line in (a).

Fig. 1: Vector flow velocity estimation results from one simulated case not used in the training and validation process. (a) Vector flow image. The lengths of the arrows indicate the flow velocity magnitude, and the angle of the arrows indicate flow direction. The color in the vessel also indicates the velocity magnitude. The maximum magnitude in this figure is 211 mm/s. (b) Velocity profiles at the axial cross-section at 3 mm in the azimuth dimension, indicated with white dashed line in (a). The estimated velocity profiles are shown in solid lines, and the ground truth profiles are shown in dashed lines.

velocity profile with high velocities near the center can be observed. The flow direction aligns well with the angle of vessel. Fig. 3(b) show the center axial cross-section of (a) at 0 mm azimuthally, indicated with the white dashed line in (a). Parabolic velocity can be observed, as expected in fully

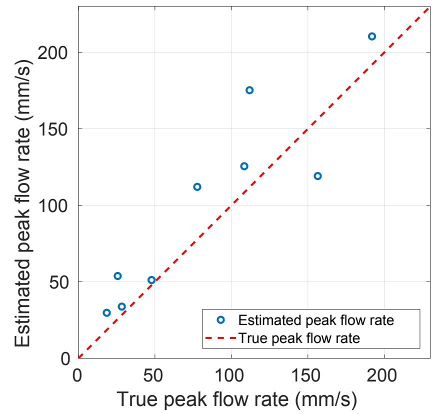

Fig. 2: Peak velocities estimated with the neural network model from data simulated at different peak flow velocities. The x-axis shows the simulated velocities (the ground truth), and the y-axis shows the estimated velocities. The red-dashed line shows where they are the equal.

developed laminar flow. Low estimation jitter is observed in the stationary tissue phantom region.

Note that, unlike in the simulation, spatially resolved ground truth velocity is not available in the experiments due to two reasons. First, no direct ground truth measurement of spatially resolved velocities is available. Secondly, the C5-2v transducer is only able to provide a 2D cross-section of the vessel, and the backscattered signals of the scattered is convolved with the point-spread-function (PSF) of the imaging system, which compounds the motion of the scatterers in the PSF.

IV. Conclusion

In this work, we proposed and demonstrated a vector flow estimation technique based on a deep neural network using beamsummed RF data. In this proof-of-concept study, the performance of the techniques was demonstrated and evaluated using Field II simulation data and flow phantom experiment data. The simulation and experimental results shows that the technique is able to provide spatially resolved quantitative vector flow estimation. In the simulation, the angle estimation and velocity magnitude estimation agree with ground truth. Parabolic axial velocity profiles can be seen in the estimates in both the simulation and the experiments. Low estimation jitter is observed in the stationary tissue region in both simulation and experiment results. In conclusion, the work demonstrated the feasibility of using the neural network based technique in vector flow estimation.

References

[1] K. L. Hansen, H. Møller-Sørensen, J. Kjaergaard, M. B. Jensen, J. T. Lund, M. M. Pedersen, T. Lange, J. A. Jensen, and M. B. Nielsen, "Analysis of systolic backflow and secondary helical blood flow in the ascending aorta using vector flow imaging," *Ultrasound in medicine & biology*, vol. 42, no. 4, pp. 899–908, 2016.

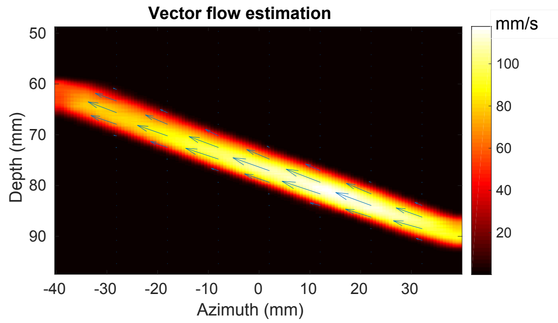

(a) Vector flow estimation results from one flow phantom experiment. The estimated flow angle is 108.88°, or equivalently, 18.88° to the surface of the phantom, which is close to the true vessel angle of 18°. The estimated peak flow velocity is 117.7 mm/s.

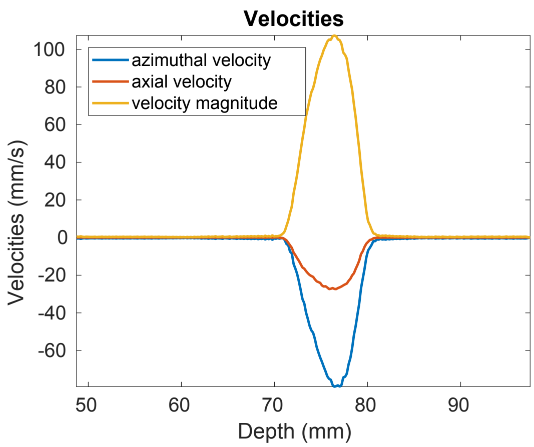

(b) Azimuth, axial velocities, and velocity magnitudes at the axial cross-section at 0 mm in the azimuth dimension, indicated with the white dashed line in (a).

Fig. 3: Vector flow velocity estimation results from one flow phantom experiment. (a) Vector flow image. The lengths of the arrows indicate the flow velocity magnitude, and the angle of the arrows indicate flow direction. The color in the vessel also indicates the velocity magnitude. The maximum magnitude in this figure is 117.7 mm/s. The estimated flow angle is 108.88°, or equivalently, 18.88° to the surface of the phantom. (b) Velocity profiles at the axial cross-section at 0 mm in the azimuth dimension, indicated with the white dashed line in (a).

[2] S. I. Nikolov and J. A. Jensen, "In-vivo synthetic aperture flow imaging in medical ultrasound," *IEEE transactions on ultrasonics, ferroelectrics, and frequency control*, vol. 50, no. 7, pp. 848–856, 2003.
[3] J. A. Jensen, "Directional Transverse Oscillation Vector Flow Estimation," *IEEE Trans. Ultrason., Ferroelect., Freq. Contr.*, vol. 64, no. 8, pp. 1194–1204, Aug. 2017.
[4] J. A. Jensen, S. I. Nikolov, A. C. Yu, and D. Garcia, "Ultrasound vector flow imagingpart ii: Parallel systems," *IEEE Trans. Ultrason., Ferroelectr., Freq. Control*, vol. 63, no. 11, pp. 1722–1732, 2016.
[5] L. N. Bohs, B. H. Friemel, and G. E. Trahey, "Experimental velocity profiles and volumetric flow via two-dimensional speckle tracking," *Ultrasound in medicine & biology*, vol. 21, no. 7, pp. 885–898, 1995.
[6] J. A. Jensen, "Field: A program for simulating ultrasound systems," *Med. Biol. Eng. Comput.*, vol. 34, Suppl. 1, pt. 1, pp. 351–353, 1996.
[7] J. A. Jensen and N. B. Svendsen, "Calculation of pressure fields from arbitrarily shaped, apodized, and excited ultrasound transducers," *IEEE Trans. Ultrason., Ferroelect., Freq. Contr.*, vol. 39, no. 2, pp. 262–267, 1992.
[8] D. Sun, X. Yang, M.-Y. Liu, and J. Kautz, "PWC-Net: CNNs for optical flow using pyramid, warping, and cost volume," in *Proceedings of the IEEE Conference on Computer Vision and Pattern Recognition*, 2018, pp. 8934–8943.
[9] D. Sun, X. Yang, M. Liu, and J. Kautz, "Models matter, so does training: An empirical study of CNNs for optical flow estimation," *IEEE Transactions on Pattern Analysis and Machine Intelligence*, pp. 1–1, 2019.
[10] A. Dosovitskiy, P. Fischer, E. Ilg, P. Häusser, C. Hazırbaş, V. Golkov, P. v.d. Smagt, D. Cremers, and T. Brox, "Flownet: Learning optical flow with convolutional networks," in *IEEE International Conference on Computer Vision (ICCV)*, 2015. [Online]. Available: http://lmb.informatik.uni-freiburg.de/Publications/2015/DFIB15
[11] A. Geiger, P. Lenz, and R. Urtasun, "Are we ready for autonomous driving? the KITTI vision benchmark suite," in *Conference on Computer Vision and Pattern Recognition (CVPR)*, 2012.
[12] D. J. Butler, J. Wulff, G. B. Stanley, and M. J. Black, "A naturalistic open source movie for optical flow evaluation," in *European Conf. on Computer Vision (ECCV)*, ser. Part IV, LNCS 7577, A. Fitzgibbon et al. (Eds.), Ed. Springer-Verlag, Oct. 2012, pp. 611–625.
[13] Y. L. Li, D. Hyun, L. Abou-Elkacem, J. K. Willmann, and J. J. Dahl, "Visualization of small-diameter vessels by reduction of incoherent reverberation with coherent flow power doppler," *IEEE transactions on ultrasonics, ferroelectrics, and frequency control*, vol. 63, no. 11, pp. 1878–1889, 2016.
[14] Y. L. Li and J. J. Dahl, "Angular coherence in ultrasound imaging: Theory and applications," *The Journal of the Acoustical Society of America*, vol. 141, no. 3, pp. 1582–1594, 2017.
[15] G. Montaldo, M. Tanter, J. Bercoff, N. Benech, and M. Fink, "Coherent plane-wave compounding for very high frame rate ultrasonography and transient elastography," *IEEE Trans. Ultrason., Ferroelect., Freq. Contr.*, vol. 56, no. 3, pp. 489–506, 2009.
[16] E. Mace, G. Montaldo, I. Cohen, M. Baulac, M. Fink, and M. Tanter, "Functional ultrasound imaging of the brain," *Nat Meth*, vol. 8, no. 8, pp. 662–664, 2011.
[17] S. Bjaerum, H. Torp, and K. Kristoffersen, "Clutter filter design for ultrasound color flow imaging," *IEEE Trans. Ultrason., Ferroelectr., Freq. Control*, vol. 49, no. 2, pp. 204–216, 2002.
[18] E. S. Chornoboy, "Initialization for improved IIR filter performance," *Signal Processing, IEEE Transactions on*, vol. 40, no. 3, pp. 543–550, 1992.
[19] Y. L. Li, D. Hyun, I. Durot, J. K. Willmann, and J. J. Dahl, "High sensitivity liver vasculature visualization using a real-time coherent flow power doppler (CFPD) imaging system: A pilot clinical study," in *2018 IEEE International Ultrasonics Symposium (IUS)*. IEEE, 2018, pp. 1–9.
[20] C. Demené, T. Deffieux, and M. Pernot, "Spatiotemporal clutter filtering of ultrafast ultrasound data highly increases Doppler and fUltrasound sensitivity," *IEEE Trans. Med. Imaging*, vol. 34, no. 11, pp. 2271–2285, 2015.